Computational Verification of So-Called Perovskite Solar Cells as PbI$_6^{4-}$-Aligned Solar Cells

Shozo Yanagida,[a,b,z] Susumu Yanagisawa,[c] Masatoshi Yanagida,[d] and Hiroshi Segawa[b]

[a]*Frontier Research Center, Osaka University, Suita, Osaka 565-0871, Japan*
[b]*Research Center for Advance Science and Technology, The University of Tokyo, Meguro-ku, Tokyo 153-8904, Japan*
[c]*Department of Physics and Earth Sciences, Faculty of Science, University of the Ryukyus, Nishihara, Okinawa 903-0213, Japan*
[d]*Environment and Energy Materials Division, National Institute for Materials Science, 1-1 Namiki, Tsukuba, Ibaraki 305-0044, Japan*

Effective sensitizing components in so-called perovskite solar cells (PSC) are lead hexaiodide (PbI$_6^{4-}$) salts of PbI$_6^{4-}$ (MeNH$_3^+$)$_n$ (n = 2∼4). Density-functional-theory-based molecular modeling (DFT/MM) of X-ray crystalline structure of PbI$_6^{4-}$/MeNH$_3^+$ salt (FOLLIB) verifies that the packing unit of FOLLIB has UV/Vis absorption spectrum at λmax = 424 nm, giving pale yellow color as complementary. DFT/MM of the horizontal component in the FOLLIB gives narrow energy gap of 0.3 eV, verifying remarkable semiconducting property through tight alignments of PbI$_6^{4-}$ components coupled with MeNH$_3^+$. DFT/MM of the central PbI$_6^{4-}$/MeNH$_3^+$ components verifies that the central component has UV/Vis absorption spectra with respective λmax = 570 nm, λmax = 762 nm and λmax = 945 nm, and plays an essential role as panchromatic sensitizers. In addition, their equilibrium geometric structures show slightly hypsochromic UV/Vis absorption spectra at respective λmax = 486 nm, λmax = 560 nm, and λmax = 563 nm as results of migration of MeNH$_3^+$ close to PbI$_6^{4-}$. DFT/MM also verifies that PbI$_6^{4-}$ components align tightly to nanocrystalline TiO$_2$ (nc-TiO$_2$) and to spiro-OMeTAD in PSC through electron density induced by van der Waals interaction. Electron density-based alignments of PbI$_6^{4-}$ components align well unidirectional and leakage-free electron diffusion leading to high open-circuit voltage in PbI$_6^{4-}$-aligned solar cells. At the same time, the semiconducting and panchromatic sensitizing layer of PbI$_6^{4-}$/MeNH$_3^+$ components contribute to excellent short-circuit photocurrent of PbI$_6^{4-}$-aligned solar cells.

Miyasaka and his group reported the first lead halide-sensitizers for photovoltaic cells, comprising the solid-state lead trihalides with perovskite structures.[1] Since then, the name "perovskite solar cell (PSC)" has been introduced to most photovoltaic research and developments using methylammonium lead trihalides [MeNH$_3$PbX$_3$, (X = I, Br, and Cl)] as sensitizing chemicals.[2] On the other hand, it was reported in 1987 that drop-wise addition of a concentrated aqueous solution of Pb(NO$_3$)$_2$ to an aqueous solution containing excess MeNH$_3^+$I$^-$ yields a black precipitate of MeNH$_3$PbI$_3$, and that the solutions of MeNH$_3$PbI$_3$ gives pale yellow crystalline solid that is composed of lead hexaiodide (PbI$_6^{4-}$), MeNH$_3^+$ and H$_2$O.[3] In addition, the crystalline structure was analyzed by X-ray crystallography and the packing unit of the crystal is now coded as FOLLIB in Cambridge Structural Data (CSD). We understand that lead hexaiodide ion (PbI$_6^{4-}$) are coordinated with methylammonium ion (MeNH$_3^+$), changed into dark colored components in polar solvent, and predict that PbI$_6^{4-}$ should play an essential role in efficient and effective molecular-structuring in perovskite-type solar cells, e.g., nanocrystalline TiO$_2$ (nc-TiO$_2$)/MeNH$_3$PbI$_3$/spiro-OMeTAD-based PSC. Our density-functional-theory-based molecular modeling (DFT/MM) verifies essential roles of molecular alignment of PbI$_6^{4-}$ components in electronic and photonic properties, i.e., high electron diffusion and diffusion length[4] and panchromatic light harvesting characteristics toward so-called PSC, i.e., PbI$_6^{4-}$-aligned solar cells.

Computational Methods

We perform DFT-based molecular modeling (DFT/MM), equivalent to the quantum mechanics/molecular mechanics (QM/MM) method, by using the B3LYP exchange-correlation functional and the 6–31G(d) basis set with Spartan'14 (Wavefunction, Inc. Irvine, CA). We investigate theoretical models of PbI$_6^{4-}$-aligned components by evaluating possible equilibrium states based on total energies (E), heats of formation (ΔE), electron energy structures and configurations of HOMO and LUMO, HOMO-LUMO energy gap, UV/Vis spectra, dipole moment and electronic charge of the components. To visualize their van der Waals and coulomb interactions, electron density structure, Mulliken charge, and electrostatic potential map are examined. We also focus on the distances between Pb and nitrogen atoms in the vicinity of MeNH$_3^+$. DFT/MM data are summarized in supplementary materials. The crystal geometry of FOLLIB is also shown in Fig. 1, which was obtained by the geometry optimization with the Vienna Ab-initio Simulation Package (VASP) code,[5] in which the lattice constants were fixed to the experimental values.[3] Details of the VASP calculation is described in supplementary materials.

Results and Discussion

Energy structure analysis for verification of semiconducting property of the MeNH$_3$PbI$_3$ –aligned layer in so-called PSC.— As we reported[6] in the previous theoretical study of electron mobility of tetramethylammonium pentaiodide and pentaiodide-based electrolytes in dye-sensitized solar cells, DFT-based single point calculations on the whole packing unit of the pale yellow PbI$_6^{4-}$ crystal (FOLLIB) are carried out. The 3D molecular structures of FOLLIB (space filling model with C60 model, electrostatic potential map in unit of kJ/mol, the VASP-optimized crystal structure, and Mulliken charge on ball and wire structure) are shown in Fig. 1.

All the 3D models show that the packing unit of FOLLIB is fully occupied by large 9 lead hexaiodide (PbI$_6^{4-}$), one of which forms a central core unit with symmetrical three types of MeNH$_3^+$ components, i.e., [(MeNH$_3^+$)$_2$-H$_2$O)$_2$, [MeNH$_3^+$-H$_2$O]$_2$, and [MeNH$_3^+$]$_2$ (see Figure S1, Tables S1). The Mulliken charge and the electrostatic potential map visualize molecular orbital-based van der Waals and coulomb interactions (vdW&Clb) in the pale yellow PbI$_6^{4-}$ salt with MeNH$_3^+$ and H$_2$O.

The molecular orbital energy structure analysis reveals that HOMO locates on the central PbI$_6^{4-}$ ion, and the almost degenerate LUMO and LUMO(+1)∼LUMO(+9) on peripheral PbI$_6^{4-}$ ions (Fig. 2).

[z]E-mail: yanagida@mls.eng.osaka-u.ac.jp
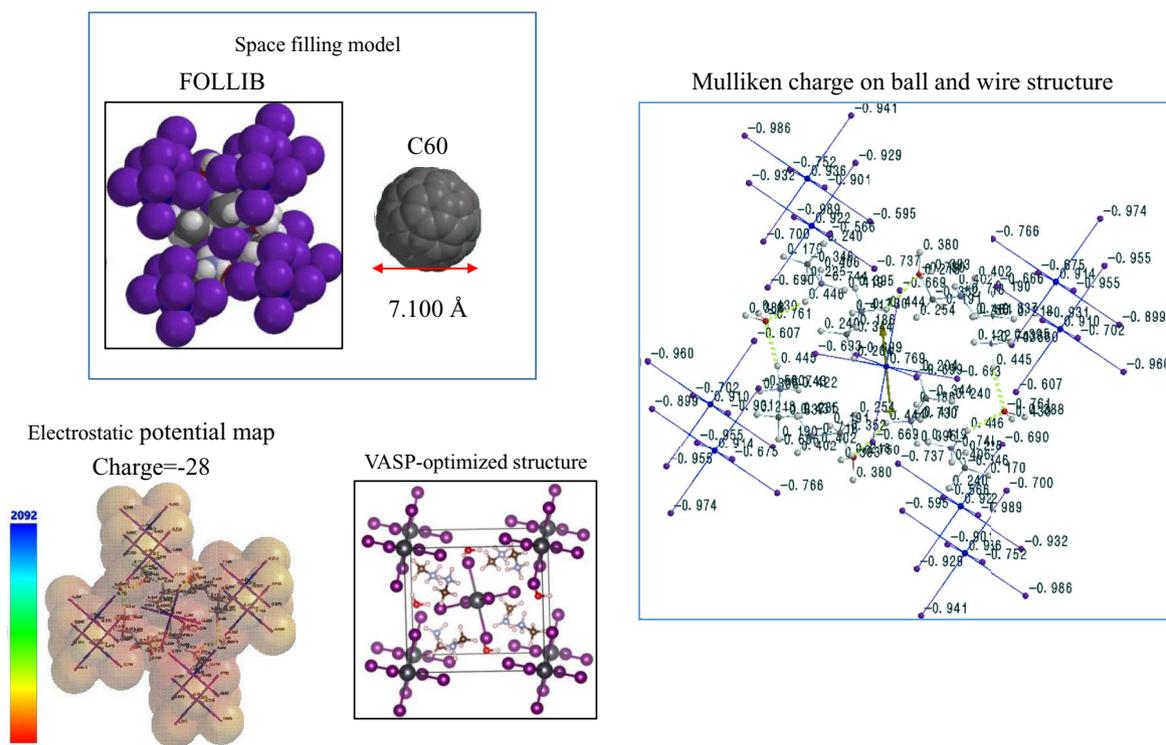
Figure 1. Space filling structure, electrostatic potential map, VASP-optimized structure and Mulliken charge of the packing unit(FOLLIB): $\{[(PbI_6)^{4-}]_9\}^{36-}\&\{[(MeNH_3^+)_2\text{-}H_2O]_2\}^{4+}\&\{[MeNH_3^+\text{-}H_2O]_2[MeNH_3^+]_2\}\}^{4+}$.

Interestingly, the energy gaps between them are small, for example, the energy difference between LUMO and LUMO(+1) (not distinguishable in the energy level diagram) is 0.01 eV, demonstrating that FOLLIB with the minimum unit of PbI_6^{4-}-aligned salt become intrinsically semiconducting at a negatively biased electron-transporting state.

For further confirmation of the semiconducting property,[2] DFT/MM of radical anion of [FOLLIB].- is carried out (Fig. S2). The molecular orbitals, aHOMO (or singly occupied molecular or-bital (SOMO)) and aLUMO, give narrow energy gap (0.17 eV) and spin density locates on peripheral PbI_6^{4-} units. The spin density map indicates distribution of the spin density on the whole structure of FOLLIB. In addition, configuration of aHOMO and aLUMO are iden-tical with those of LUMO(0) and the second LUMO (LUMO(+1)) in FOLLIB (the stationary state, see Fig. 2).

To deepen understanding on the semiconducting property induced by the linear alignment of PbI_6^{4-} in terms of the computed electronic

| Name	ΔE(kcal/mol)	LUMO(eV)	HOMO(eV)	Energy gap(eV)	LUMO(+1)(eV)	charge
FOLLIB	5799.51	35.89	32.89	3.0	35.9	-28
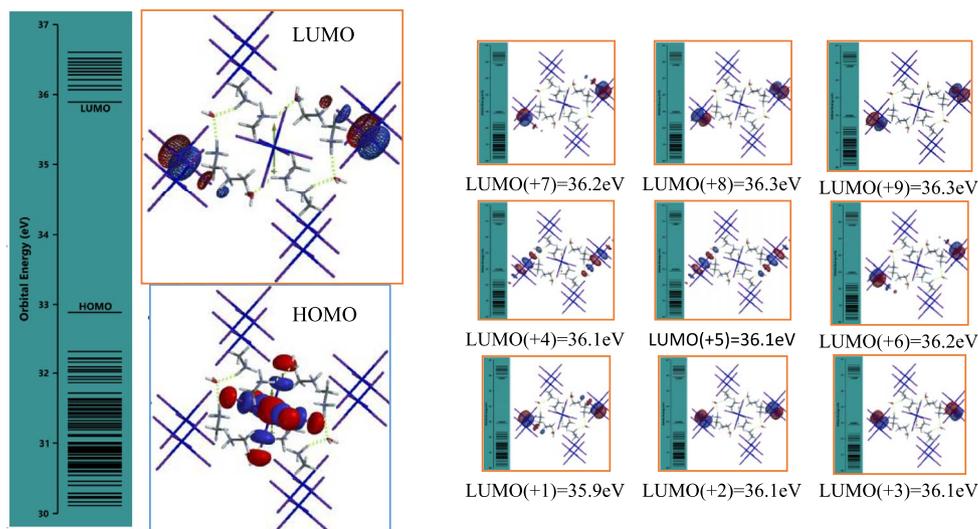
Figure 2. molecular orbital energy structure of the packing unit FOLLIB: $\{[(PbI_6)^{4-}]_9\}^{36-}\&\{[(MeNH_3^+)_2\text{-}H_2O]_2\}^{4+}\&\{[MeNH_3^+\text{-}H_2O]_2[MeNH_3^+]_2\}\}^{4+}$.

| Density(DFT-based structure) | LUMO(0) LUMO(+1) | Mulliken charge |
| HOMO(0) HOMO(+1) | Electrostatic potential map |

E(kcal/mol)	LUMO(eV)	HOMO(eV)	Energy gap(eV)	LUMO(+1)(eV)	charge
-1706.96	3.67	3.37	0.3[*1]	**3.7**	**+4**
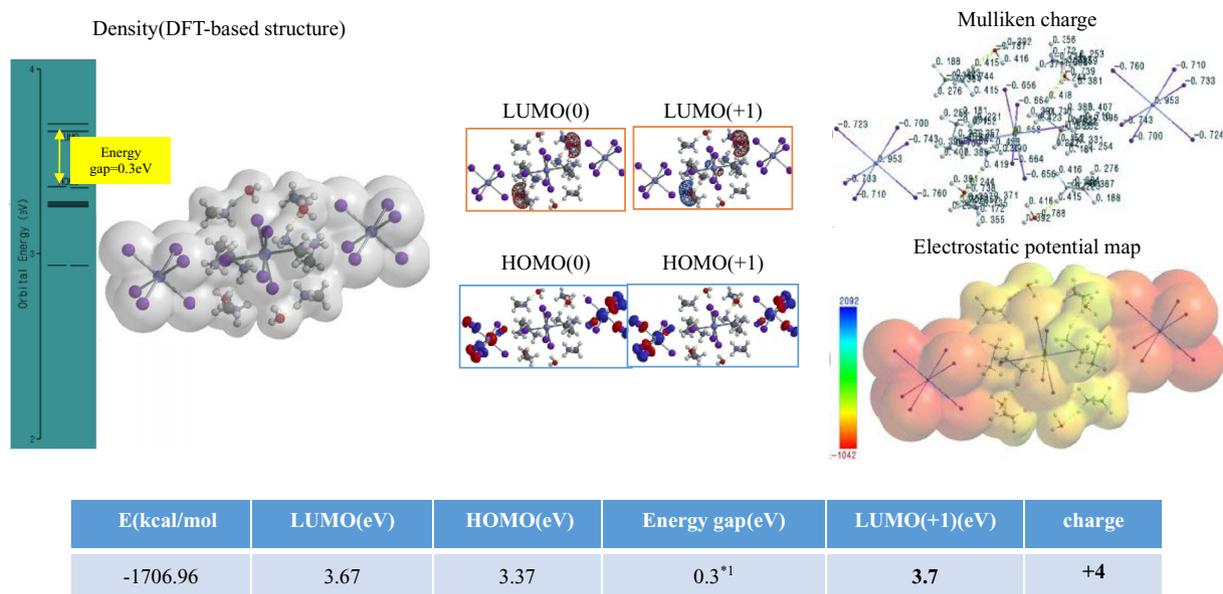
[*1] HOMO->LUMO, λmax = 14892 nm (f = 0.0026), HOMO->LUMO 56%

Figure 3. Molecular orbital energy structure of oblique plain unit in FOLLIB: $[(PbI_6)^{4-} \& ((MeNH_3^+)_2\text{-}H_2O)_2 (MeNH_3^+\text{-}H_2O)_2 \& (MeNH_3^+)_2 / (PbI_6)^{4-}]_2]^{4-}$.

structure, the oblique plain unit in FOLLIB, $[(PbI_6^{4-})_3, ((MeNH_3^+)_2\text{-}H_2O)_2 \& (MeNH_3^+\text{-}H_2O)_2 \& (MeNH_3^+)_2]^{4-}$ is analyzed as well (Fig. 3 and Table S1).

The density structure suggests that three PbI_6^{4-} ions align tightly via vdW&Clb and the plus 4 charge distributes over whole of the ion, while negative charge locates on the peripheral PbI_6^{4-} and positive charge on the central one (quantitatively, see the Mulliken charge). Surprisingly, the HOMO-LUMO energy gap is calculated to be 0.3 eV. In addition, HOMO locates on PbI_6^{4-} and LUMO on $MeNH_3^+$, which are almost degenerate, and the energy gap between LUMO(0) and LUMO(+) is 0.03 eV.

Thus, we confirm that DFT/MM-based energy and configuration analysis for LUMO and second LUMO(+) is a measure for semi-

conducting electron diffusion property.[6–8] Accordingly, DFT/MM of FOLLIB predicts that PbI_6^{4-} will align tightly via vdW&Clb, giving excellent semiconducting electron diffusion path over the whole of the PbI_6^{4-}-aligned layers of PSC, as found for polyiodide electrolytes in dye-sensitized solar cells.[9]

Verification of $PbI_6^{4-}/MeNH_3^+$ components as dark colored (panchromatic) sensitizers.—DFT/MM-based UV/Vis spectrum analysis predicts that FOLLIB has UV/Vis absorption maximum at λmax = 424 nm (intensity of 0.00315; see Fig. 4), which is consistent with the energy gap of 3.0 eV. Pale yellow color of the crystalline salt is complementary color of the absorption at λmax = 424 nm

λmax = 424 nm (0.00315)
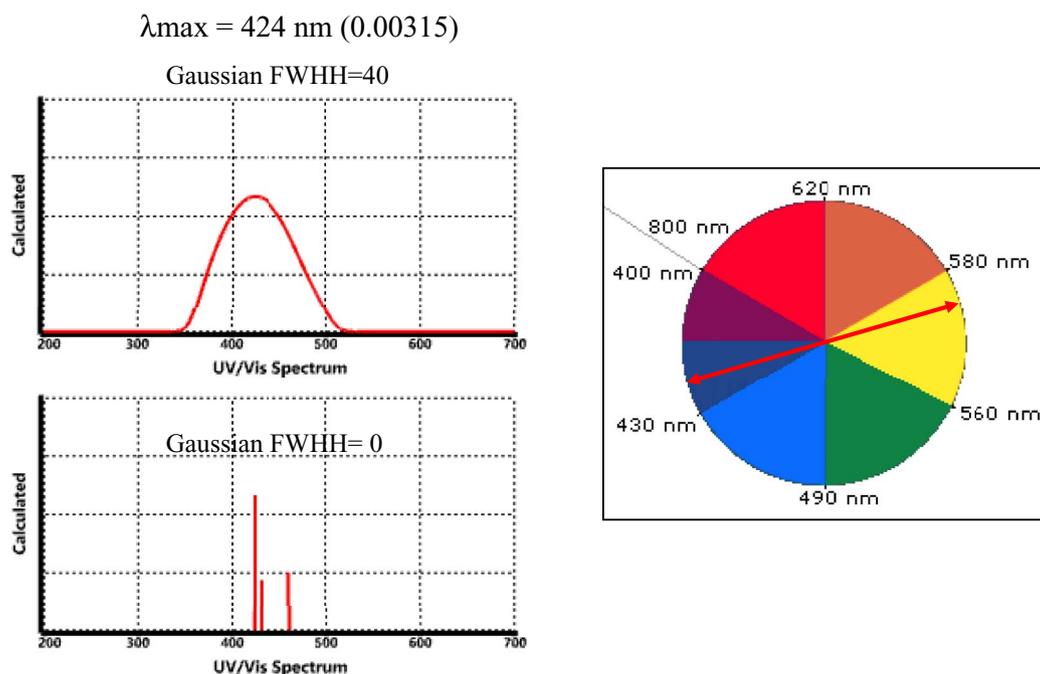
Figure 4. DFT-based UV/Vis spectrum of FOLLIB.
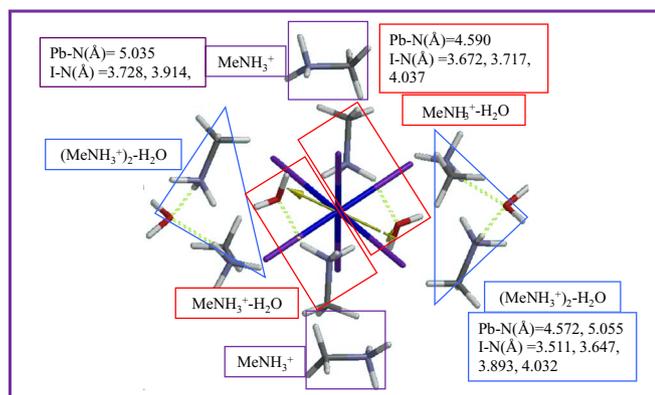
Figure 5. Structure of $[(MeNH^{3+})_2\text{-}H_2O]_2\&[MeNH_3^+\text{-}H_2O]_2\&[MeNH_3^+]_2\&PbI_6^{4-}$ in the central core unit of FOLLIB.

(Fig. 4). We apply the reliable DFT/MM-based UV/Vis spectrum analysis to modeling of other $PbI_6^{4-}/MeNH_3^+$ salts.

The pale yellow salt ($PbI_6^{4-}\&MeNH_3\&H_2O$) is soluble in polar solvent, forming dark color solution.[3] In order to predict structures of red-, green- or blue-colored $PbI_6^{4-}/MeNH_3^+$ salts, we use DFT/MM to elucidate the effects of the $PbI_6^{4-}/MeNH_3^+$ pairs in the core unit of FOLLIB. Careful examination reveals that PbI_6^{4-} is surrounded by the outermost $[MeNH_3^+]$ (the Pb-N interatomic distance (d(Pb-N)) = 5.035Å), the intermediate $[(MeNH_3^+)_2\text{-}H_2O]$ (d(Pb-N) = 5.055, 4.572Å), and the innermost $[MeNH_3^+\text{-}H_2O]$ (d(Pb-N) = 4.590Å). The iodine-ammonium (I-N) interatomic distances in all the $MeNH_3^+$ species range from 3.5 to 4.1 Å (Fig. 5).

The central core unit, PbI_6^{4-}, and PbI_6^{4-} components surrounded symmetrically by $[(MeNH_3^+)_2\text{-}H_2O]_2$, $[MeNH_3^+\text{-}H_2O]_2$, or $[MeNH_3^+]_2$ are modeled with DFT/MM for UV/Vis absorption spectra (Table I).

All of the formation energies (ΔE) are negative, suggesting that the examined salt ions are all thermodynamically stable. The energy structures of LUMO(0) and LUMO(+1), with their small energy difference, predict that all of the salts should have semiconducting electron diffusion property under a negatively biased condition. As for the UV/Vis spectra, however, the PbI_6^{4-} salts with the innermost $[MeNH_3^+\text{-}H_2O]$ results in blue-shifted λmax that ranges from 269nm to 309nm. On the other hand, the PbI_6^{4-} salts with the outermost $[MeNH_3^+]$, or intermediate $[(MeNH_3^+)_2\text{-}H_2O]$ gives red-shifted λmax, indicating that when $MeNH_3^+$ locates far enough from PbI_6^{4-}, the salt ions will give red-shifted UV/Vis absorption spectra.

The interatomic distance between Pb atom of PbI_6^{4-} and N atom in the outermost Me-NH_3^+ is optimized by stepwise DFT/MM of water-free $[MeNH_3^+I^-]$ (Fig. S10) and water-free $[PbI_6^{4-}\&MeNH_3^+]$ (Fig. S11). The iodine-ammonium nitrogen (I-N) distance of 3.184 Å and the lead-ammonium (Pb-N) distance of 6.414 Å are obtained. Based on the bond distance in $[PbI_6^{4-}\&MeNH_3^+]$, unsymmetrical di-ammonium-salt SPE-1$[PbI_6^{4-}\&(MeNH_3^+)_2]$ (Fig. S12), symmetrical di-ammonium-salt SPE-2$[PbI_6^{4-}\&(MeNH_3^+)_2]$ (Fig. S13), symmetrical tri-ammonium-salt, SPE$[PbI_6^{4-}\&(MeNH_3^+)_3]$ (Fig. S14), and symmetrical tetra-ammonium salt SPE$[PbI_6^{4-}\&(MeNH_3^+)_4]^0$ (Fig. S15) are molecularly modeled by single point energy (SPE) calculation of their molecular-mechanics-optimized (MMFF) structures (Table S3).

The interatomic distances between lead atom of PbI_6^{4-} and nitrogen atom of $MeNH_3^+$ range from 6.043 to 6.387 Å for all of the calculated PbI_6^{4-} salts. The Pb-N distances are about 1 Å longer than those of the components in FOLLIB. DFT/MM-based UV/Vis

Table I. Energy structures of $MeNH_3^+$ -aligned PbI_6^{4-} units in the core of FOLLIB.

$PbI_6^{4-}/MeNH_3^+$ salts in FOLLIB core components	ΔE (kcal/mol)	Pb-N (Å)	LUMO (eV)	LUMO(+1) (eV)	HOMO (eV)	Energy gap (eV)	λmax (nm) (intensity) Allowed transition (%) λ (nm) (Intensity) HOMO-LUMO contribution	Ref.
[center core unit] $^{4+}$	−727.53	4.572 4.590 5.035 5.055	−8.67	−8.6	−13.74	5.07 (245 nm)	269.35(0.0954) HOMO→LUMO(+1) 94% 278.44(0.0692) HOMO→LUMO 94%	Fig. S2
SPE PbI_6^{4-}	—	—	12.61	12.7	7.26	5.35 (231 nm)	260.74(0.1036) HOMO→LUMO 89%	Fig. S3
$[PbI_6^{4-}\&((MeNH_3^+)_2\text{-}H_2O)_2\&(MeNH_3^+\text{-}H_2O)_2]^{2+}$	−912.47	4.572 4.590 5.055	−4.53	4.5	−9.37	4.84 (256 nm)	263.63(0.1101) HOMO→LUMO 100%	Fig. S4
$[PbI_6^{4-}\&(MeNH_3^+\text{-}H_2O)_2\&(MeNH_3^+)_2]$	−761.03	4.590 5.035	0.08	0.1	−3.66	3.74 (332 nm)	346.12(0.0035) HOMO(−1)→LUMO(+1) 84% 380.99(0.000) HOMO→LUMO 99%	Fig. S5
$[PbI_6^{4-}\&(MeNH_3^+\text{-}H_2O)_2]^{2-}$	−545.99	4.590	5.7	5.7	1.17	4.53 (274 nm)	309.26(0.0136) HOMO→LUMO(+1) 85% 309.17(0.0003) HOMO→LUMO 85%	Fig. S6
$[PbI_6^{4-}\&((MeNH_3^+)_2\text{-}H_2O)_2\&(MeNH_3^+)_2]^{2+}$	−810.2	4.572 5.035 5.055	5.48	5.5	5.04	0.44 (2818 nm)	2349.67(0.0284) HOMO(−1)→LUMO 62% 2683.48(0.000) HOMO→LUMO 23%	Fig. S7
$[PbI_6^{4-}\&((MeNH_3^+)_2\text{-}H_2O)_2]$	−776.93	4.572 5.055	−0.79	−0.8	−3.69	2.9 (428 nm)	417.25(0.0218) HOMO(−3)→LUMO(+1) 63% 505.10(0.000) HOMO→LUMO 100%	Fig. S8
$[PbI_6^{4-}\&((MeNH_3^+)_2]^{2-}$	−481.85	5.035	4.35	4.4	1.58	2.77 (448 nm)	456.13(0.0109) HOMO(−1)→LUMO(+1) 86% 540.62(0.000) HOMO→LUMO 100%	Fig. S9
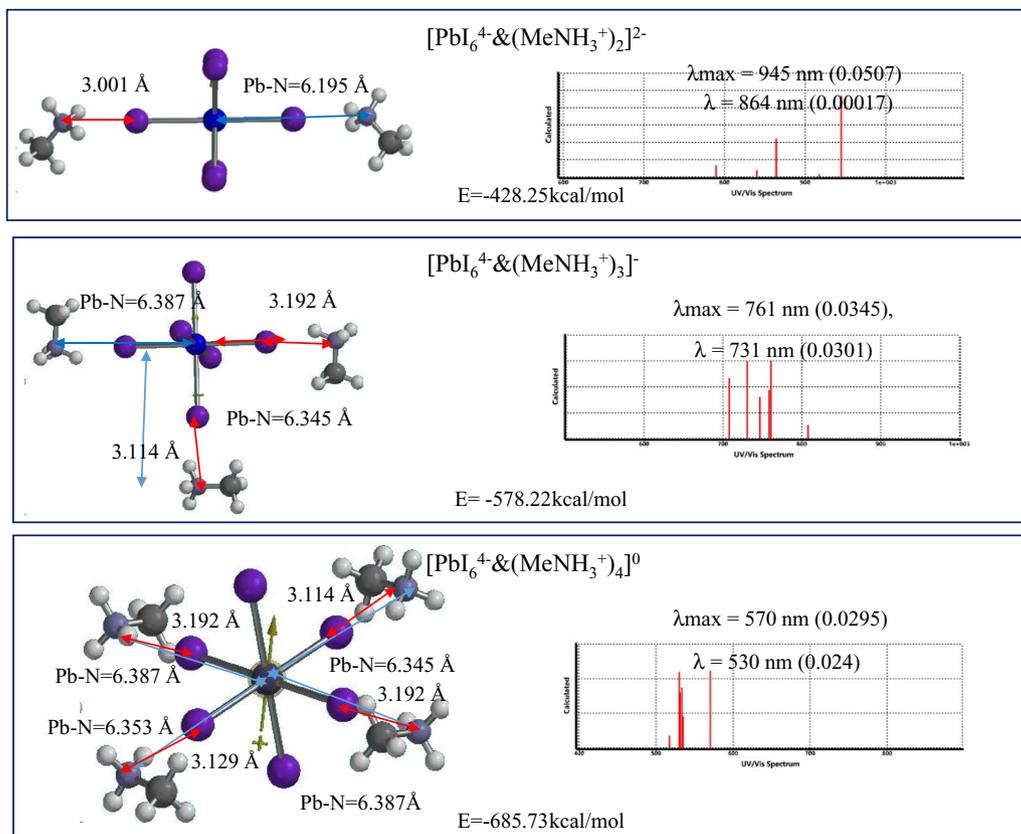
Figure 6. UV/Vis spectra calculated by single point DFT/MM of H_2O-free symmetrical PbI_6^{4-}&$MeNH_3^+$ salts.

spectra of SPE[PbI_6^{4-}&($MeNH_3^+$)$_2$],[2] SPE[PbI_6^{4-}&($MeNH_3^+$)$_3$]$^-$, and SPE[PbI_6^{4-}&($MeNH_3^+$)$_4$]^0, are shown in Figure 6. Interestingly, UV/Vis absorption spectra have the absorption maxima (λmax) that range from visible region to near infrared region.

Given the high absorption intensity of 0.02~0.05 at λmax, molecular components of SPE[PbI_6^{4-}&($MeNH_3^+$)$_3$]$^-$and SPE[PbI_6^{4-}&($MeNH_3^+$)$_4$]^0 will give dark green and dark blue color, respectively as complementary color. Accordingly, we propose that water-free PbI_6^{4-}&$MeNH_3$ molecular components should work panchromatic molecularly-layered sensitizers, i.e., quantum dot sensitizers.

Figure 7 shows UV/Vis spectra of three equilibrium geometry (EQG)-based stabilized [PbI_6^{4-}&($MeNH_3^+$)$_4$]^0. EQG-1[PbI_6^{4-}($MeNH_3^+$)$_4$]^0 ($\Delta E = -697.37$ kcal/mol), where the ionic configurations in all of $MeNH_3^+$ are frozen, gives an absorption of λmax = 486 nm (intensity: 0.0278), while SPE[PbI_6^{4-}($MeNH_3^+$)$_4$]^0 ($\Delta E = -685.73$ kcal/mol) an absorption of λmax = 570 nm (intensity: 0.029) (Fig. 6). Further, EQG-2[PbI_6^{4-}($MeNH_3^+$)$_4$]^0 ($\Delta E = -728.28$ kcal/mol), with the ions in one $MeNH_3^+$ allowed to relax, results in blue-shift of λmax = 429 nm (intensity: 0.0318). In this case, the distance Pb-N at unfrozen $MeNH_3^+$ becomes shorter (4.641 Å) than that in EQG-1. In addition, EQG-3[PbI_6^{4-}($MeNH_3^+$)$_4$]^0 ($\Delta E = -797.27$ kcal/mol), where all $MeNH_3^+$ ions are unfrozen, gives the most blue-shifted absorption of λ = 280nm (intensity: 0.0318). The Pb-N bond distances are shortened in EQG-3, ranging from 4.086 to 4.161 Å. The configuration of HOMO and LUMO locate on PbI_6^{4-}, which are comparable to those of PbI_6^{4-} in FOLLIB that has the blue-shifted λmax = 261 nm (intensity: 0.104) (Fig. S3).

PSC researchers often observe color change from black to yellowish red of PSC devices. The gradual color change was also reported under high temperature conditions.[10] Recently, it was reported that PbI_6^{4-} has a tendency to be stabilized by the change in geometri-

cal configuration of $MeNH_3^+$ in the crystal.[11] The above-mentioned DFT-based spectral modeling will explain the changes in color and chemical structures.

Verification of tight PbI_6^{4-}-alignments on nc-TiO$_2$.—The most remarkable characteristic of so-called perovskite solar cells is their high open-circuit voltage (Voc = ~1 eV). In the case of PSC devices composed of nc-TiO$_2$/PbI_6($MeNH_3$)$_4$/spiro-OMeTAD, PbI_6^{4-}-components must be aligned tightly at the interface of nc-TiO$_2$ and spiro-OMeTAD molecular layers through van der Waals and coulomb interactions (vdW&Clb). The tight alignments of PbI_6^{4-} should also enhance short-circuit photocurrent (Jsc; ~20 mA/cm^2) and fill factor, leading to excellent performance of the PSC devices. In other words, unidirectional electron diffusion occurs both on nc-TiO$_2$ and on spiro-OMeTAD layers in the PSC devices, minimizing resistance loss in photoelectron energy conversion processes. Taking into account the enhanced van der Waals and coulomb interactions between the PbI_6^{4-}-components, we apply DFT/MM to verify their electron density-based interactions with Yamashita-Jono anatase TiO$_2$ model of [(OH)Ti$_9$O$_{19}$H] (Figs. S19 and S20).

DFT/MM of PbI_6^{4-}-aligned nc-TiO$_2$ interface of [(OHTi$_9$O$_{18}$H)//Pb(II)I$_6^{4-}$] is performed by placing Pb(II)I$_6^{4-}$ in the van der Waals distances from Yamashita-Jono anatase TiO$_2$ model of [(OH)Ti$_9$O$_{19}$H][8] by taking into account the positive potential at central part of electrostatic potential map of [OHTi$_9$O$_{18}$H] (Figs. S19 and S21). Interestingly, the small HOMO-LUMO energy gap of 0.33 eV in the interface model of [(OHTi$_9$O$_{18}$H)//Pb(II)I$_6^{4-}$] and the energy gap between LUMO(+) and LUMO(0) of 0.07 eV corroborates high electron diffusion at interfaces between nc-TiO$_2$ and Pb(II)I$_6^{4-}$.

Further, neutral PbI_6^{4-}-aligned nc-TiO$_2$ interface modeling of (OH)Ti$_9$O$_{19}$H//($MeNH_3^+$)$_4$//Pb(II)I$_6^{4-}$ is carried out by introducing four molecules of $MeNH_3^+$ to hydrogen-bond to the above-mentioned

EQG-based Modeling where all MeNH$_3^+$are frozen.

EQG-1[PbI$_6^{4-}$(MeNH$_3^+$)$_4$]^0

6.345 Å
6.353 Å
6.387 Å
6.353 Å

λmax = 486 (0.0278)
λ = 462 (0.0214)

E= -697.37kcal/mol

EQG-based Modeling where one MeNH$_3^+$ is unfrozen.

EQG-2[PbI$_6^{4-}$(MeNH$_3^+$)$_4$]^0

6.345 Å
6.387 Å
6.345 Å   4.641 Å   Non-frozen

λmax = 429 (0.0318)
λ = 456 (0.0043)

E= -728.28kcal/mol

Molecular modeling of the SPE-based structure where all MeNH$_3^+$ are unfrozen.

EQG-3[PbI$_6^{4-}$(MeNH$_3^+$)$_4$]^0

4.129 Å
4.098Å   4.086 Å
4.161 Å

λmax = 280 nm (0.144),

E= -797.27kcal/mol

Figure 7. UV/Vis spectra obtained from equilibrium geometry (EQG) of SPE[PbI$_6^{4-}$&(MeNH$_3^+$)$_4$]^0.

(MeNH$_3$)$_4$ sre introduced to have hydrogen bonds with nc-TiO$_2$ and OH on nc-TiO$_2$ model surface

O-H$_3$N(Å)= 2.292, 2.183

MMFF

O-H$_3$N(Å)= 2.146, 1.712, 1.726, 2.022.

O-H$_3$N(Å)= 2.804, 2.255

O-H$_3$N(Å)= 2.277, 1.676,

LUMO=-4.36eV

TiO-H$_3$N(Å)= 2.255(H-bond) , 2.176(H-bond)

Ti-PbI(Å)= 3.288, 3.589,

TiO-H$_3$N(Å)= 2.277, HO-H$_3$N(Å)=1.676(H-bond), 1.483

Energy gap(eV)=0.36
LUMO(+)(eV)=-4.3

HOMO=-4.72eV

Electrostatic potential map

Dipole 21.06debye (arrow)
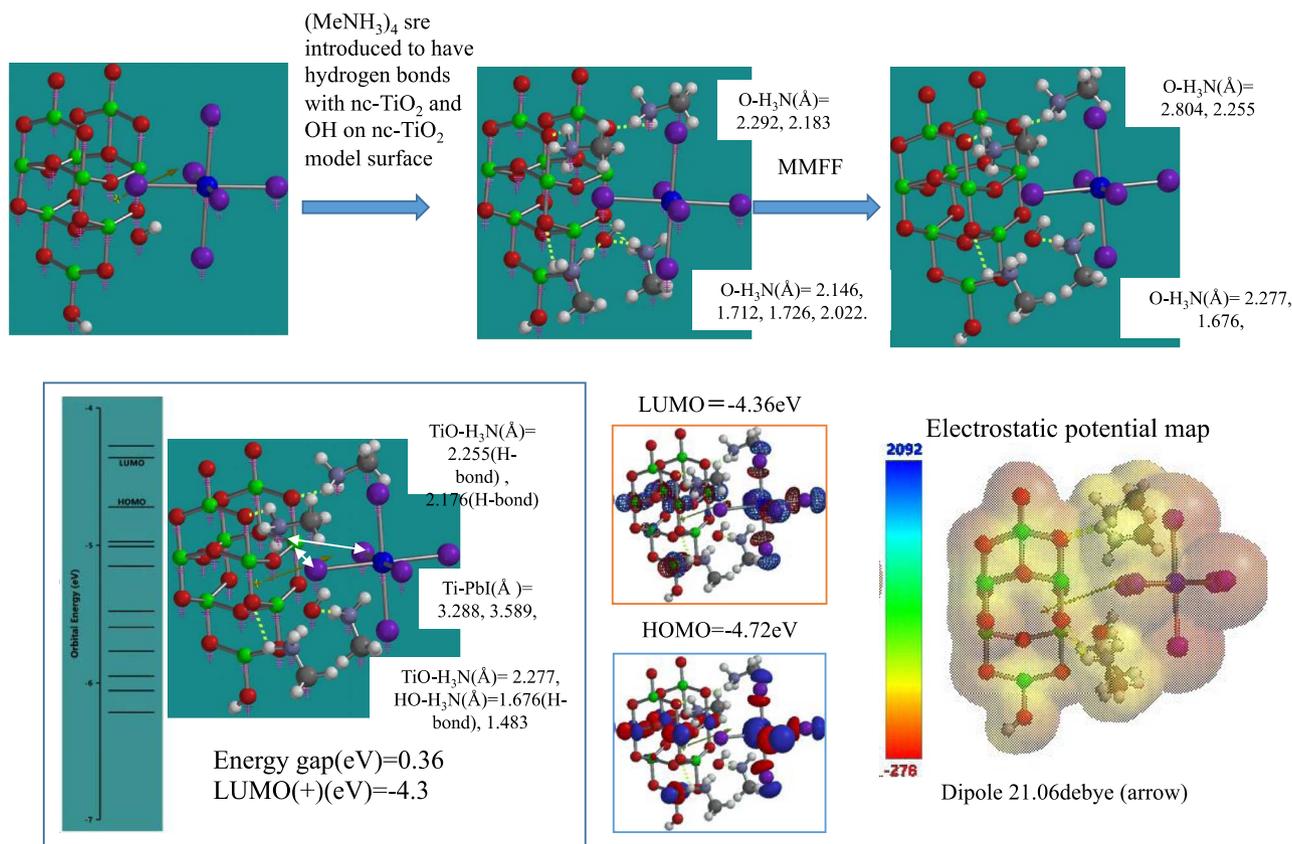
Figure 8. Molecular modeling scheme of single point energy calculations for an interface model [nc-TiO$_2$&(MeNH$_3$)$_4$&PbI$_6^{4-}$] and energy structure analyses.

Density(DFT-based structure)

LUMO

HOMO

Electrostatic potential map

Pb-N(Å)=8.568

Dipole 56.48debye (arrow)
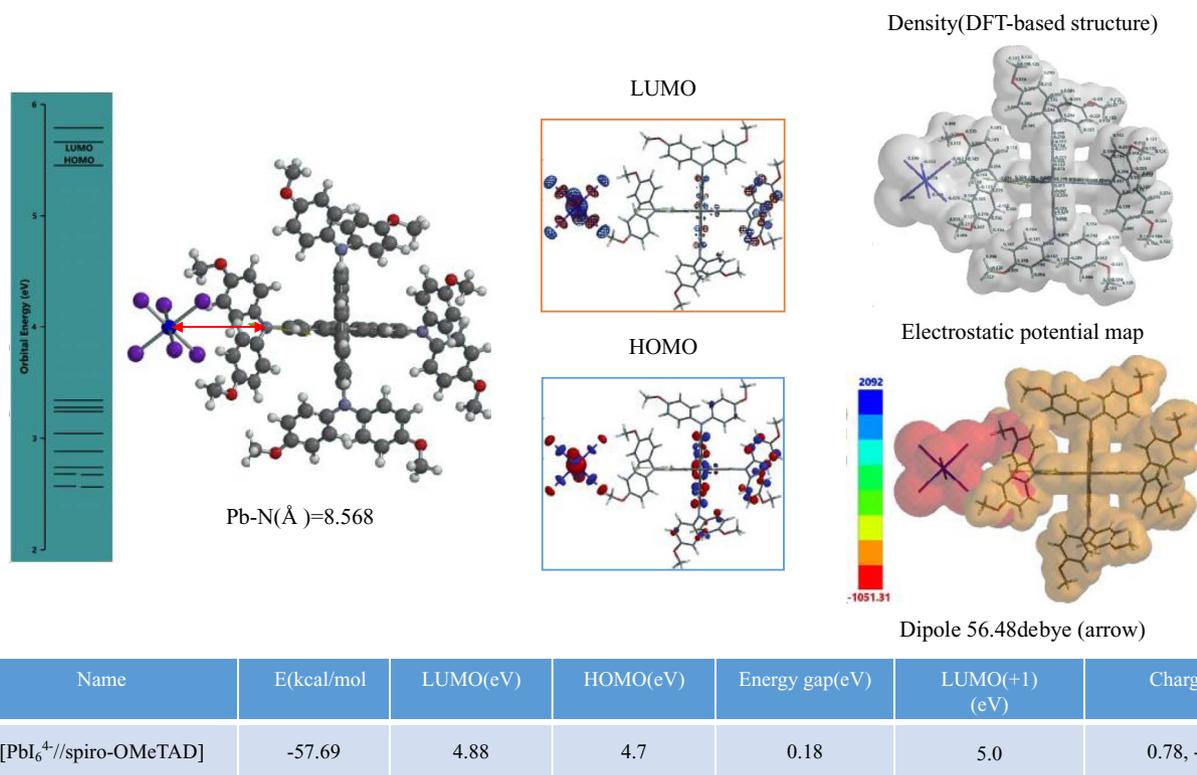
Name	E(kcal/mol)	LUMO(eV)	HOMO(eV)	Energy gap(eV)	LUMO(+1) (eV)	Charge
[PbI$_6$$^{4-}$//spiro-OMeTAD]	-57.69	4.88	4.7	0.18	5.0	0.78, -4

Figure 9. Molecular modeling of an interface of spiro-OMeTAD, Pb(II)I$_6$$^{4-}$ &spiro-OMeTAD.

model of (OH)Ti$_9$O$_{18}$H//PbI$_6$$^{4-}$ (Fig. 8, Fig. S22). The configurations of HOMO and LUMO are similar, and the HOMO-LUMO energy gap of 0.36 eV and the small energy gap between LUMO(+) and LUMO(0) of 0.06 eV are also found.

It is worth noting that, during the stepwise molecular modeling, the indication of a hydrogen bond between the neighboring OH and NH$_3$$^+$ group disappear, which may be ascribed to the change in the bond distance either larger than 2.2 Å or shorter than 1.7 Å. The electron density-based tight interaction of PbI$_6$$^{4-}$ constitutes the molecular interface with nc-TiO$_2$, in which a non-covalent interaction is involved, with the narrow energy gap. The narrow energy gap indicates high electron diffusion at the interface between PbI$_6$$^{4-}$ and nc-TiO$_2$.

The energy structures of (OH)Ti$_9$O$_{19}$H and its radical anion, [(OH)Ti$_9$O$_{19}$H]$^{.-}$ reveals that the energy gap of 0.43 eV between LUMO and LUMO(+) of [OHTi$_9$O$_{19}$H] (Fig. S19) and the energy gap of 0.83 eV of the radical anion (Fig. S20) are very narrow, which validates high electron diffusion at electron accepted state of nc-TiO$_2$ (Table S4).

Verification of Tight PbI$_6$$^{4-}$-alignments on spiro-OMeTAD.—Recently, highly disordered amorphous-state spiro-OMeTAD was found to crystallize and remarkably enhance charge-carrier transport via molecular alignment in thin spiro-OMeTAD layers, and their origin was discussed in view of electronic structure calculations.[12] DFT/MM of spiro-OMeTAD using Spartan verifies the excellent charge transport, and predicts crystallization of the standing spiro-OMeTAD. The charge transport, i.e., electron diffusion is validated by the small energy gap between LUMO(0) and LUMO(+) of the neutral spiro-OMeTAD (Fig. S23) and by the energy gap (0.64 eV) of the electron-accepted-state spiro-OMeTAD (Table S4, Fig. S24). The degenerate HOMO and LUMO of spiro-OMeTAD suggests molecular alignment through three-dimensional interactions between the HOMO and the LUMO, and crystallization (Fig. S23).

The tight interaction of PbI$_6$$^{4-}$ with charge-transporting spiro-OMeTAD is verified on the basis of DFT/MM of PbI$_6$$^{4-}$-aligned spiro-OMeTAD; [PbI$_6$$^{4-}$//spiro-OMeTAD] (Fig. 9). DFT/MM is carried out

after introducing PbI$_6$$^{4-}$ at the van der Waals distance from the center of spiro-OMeTAD. Configurations of LUMO and HOMO is identical, resulting in narrow energy gap of 0.18 eV, and the electron density structure, Mulliken charge and electrostatic potential map verifies that the interface layer become non-covalently bonded, and unidirectional electron diffusion should occur via electron density at the interface.

Conclusions

DFT/MM of nc-TiO$_2$/MeNH$_3$PbI$_3$/spiro-OMeTAD-based PSC verifies that Pb(II)I$_6$$^{4-}$ ions play an essential role in providing panchromatic sensitizer and excellent electron diffusive interface structures at nc-TiO$_2$ layers on anodes and at spiro-OMeTAD layers on cathodes of the PSC. The neutral [PbI$_6$$^{4-}$&(MeNH$_3$$^+$)$_4$] salt and the negatively charged ion [PbI$_6$$^{4-}$&(MeNH$_3$$^+$)$_3$] are verified to have strong UV/Vis absorption at λmax = 570 nm and 760 nm, respectively. In addition, both the species will become semi-conducting at electron-accepted state, i.e., under negatively biased working conditions. The alignment of PbI$_6$$^{4-}$ in so-called PSC devices is visualized using electrostatic potential maps of PbI$_6$$^{4-}$ components, in which the PbI$_6$$^{4-}$–CH$_3NH_2$$^+$ complexes are arranged via the non-covalent electrostatic and van der Waals attraction between the electron distributions at the sites of the complexes, with their electrostatic potentials identically ranging from −200 to 200 kJ/mol (−2 to 2 eV) (Fig. 10).

Panchromatic sensitizer of (MeNH$_3$$^+$)$_4$//PbI$_6$$^{4-}$ as quantum dots are sandwiched by nc-TiO$_2$//[(MeNH$_3$$^+$)$_4$Pb(II)I$_6$$^{4-}$] on anodes and the (MeNH$_3$$^+$)$_4$-covered interface of (MeNH$_3$$^+$)$_4$//PbI$_6$$^{4-}$ //spiro-OMeTAD, rationalizing that photo-electron produces effectively on quantum dots, (MeNH$_3$$^+$)$_4$//PbI$_6$$^{4-}$ and electron transport should occur unidirectionally at both semiconducting nc-TiO$_2$ and spiro-OMeTAD layers under panchromatic light irradiance. DFT/MM verifies excellent perovskite solar cells as PbI$_6$$^{4-}$-quantum dot solar cells rather than a model p-i-n diode solar cell.[13] The long-term stability issues may concern gradual structural change of the salt-like quantum dots.
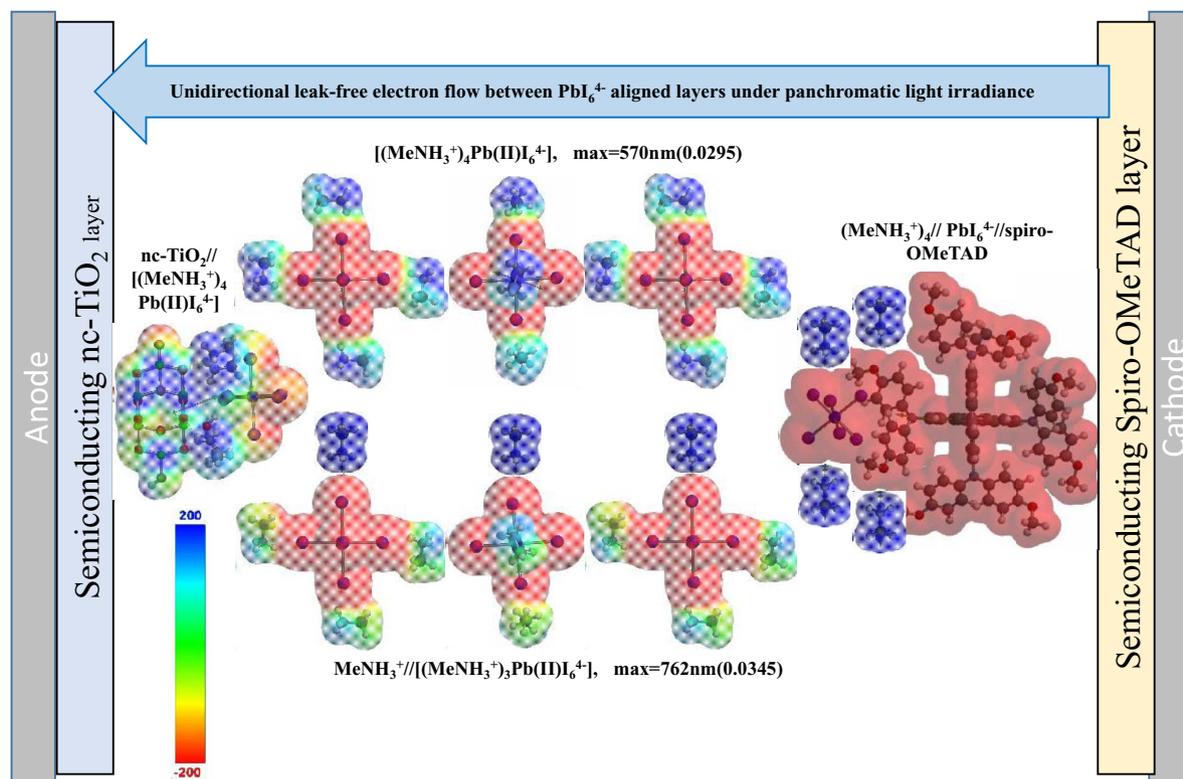
Figure 10. Electrostatic-potential based PbI$_6^{4-}$ alignment in nc-TiO$_2$ /MeNH$_3$ PbI$_3$/spiro-OMeTAD-based PSC.

References

1. A. Kojima, K. Teshima, Y. Shirai, and T. Miyasaka, *J. Am. Chem. Soc.*, **131**, 6050 (2009).
2. M. Jacoby, *Chem. Eng. News*, **94**, 30 (2016); Y. Yuan and J. Huang, *Acc. Chem. Res.*, **49**, 286 (2016); T. C. Sum, N. Mathews, G. Xing, S. S. Lim, W. K. Chong, D. Giovanni, and H. A. Dewi, *Acc. Chem. Res.*, **49**, 294 (2016); J. S. Manser, M. I. Saidaminov, J. A. Christians, O. M. Bakr, and P. V. Kamat, *Acc. Chem. Res.*, **49**, 330 (2016); W. Chen, Y. Wu, Y. Yue, J. Liu, W. Zhang, X. Yang, H. Chen, E. Bi, I. Ashraful, M. Grätzel, and L. Han, *Science*, **350**, 944 (2015); H. Kim, K-G. Lim, and T-W. Lee, *Energy Environ. Sci.*, **9**, 12 (2016).
3. B. R. Vincent, K. N. Robertson, T. S. Cameron, and O. Knop, *Can. J. Chem.*, **65**, 1042 (1987).
4. G. Hodes, *Science*, **342**, 317 (2013); X. -Y. Zhu and V. Podzorov, *J. Phys. Chem. Lett.*, **6**, 4758 (2015); J. Xia and S. Yanagida, *Solar Energy*, **85**, 3143 (2011); S. Yanagida, Y. Yu, and K. Manseki, *Acc. Chem. Res.*, **42**, 1827 (2009).
5. G. Kresse and J. Furthmüller, *Comput. Mater. Sci.*, **6**, 15 (1996); G. Kresse and J. Furthmüller, *Phys. Rev. B*, **54**, 11169 (1996).
6. S. Yanagida, S. Yanagisawa, and H. Segawa, *J. Electrochem. Soc.*, **162**, E263 (2015).
7. S. Yanagida, K. Manseki, and H. Segawa, *Electrochim. Acta*, **179**, 169 (2015).
8. S. Yanagida, S. Yanagisawa, K. Yamashita, R. Jono, and H. Segawa, *Molecules*, **20**, 9732 (2015).
9. F. C. Küpper, M. C. Feiters, B. Olofsson, T. Kaiho, S. Yanagida, M. B. Zimmermann, L. J. Carpenter, G. W. Luther III, Z. Lu, M. Jonsson, and L. Kloo, *Angew. Chem. Int. Ed.*, **50**, 11598 (2011).
10. G. E. Eperon, S. D. Stranks, C. Menelaou, M. B. Johnston, L. M. Herz, and H. J. Snaith, *Energy Environ. Sci.*, **7**, 982 (2014).
11. M. T. Weller, O. J. Weber, P. F. Henry, A. M. Di Pumpoac, and T. C. Hansen, *Chem. Commun.*, **51**, 4180 (2015).
12. D. Shi, X. Qin, Y. Li, Y. He, C. Zhong, J. Pan, H. Dong, W. Xu, T. Li, W. Hu, J-L. Brédas, and O. M. Bakr, *Sci. Adv.*, **2**, e1501491 (2016).
13. K. Miyano, N. Tripathi, M. Yanagida, and Y. Shirai, *Acc. Chem. Res.*, **49**, 303 (2016).